Nano-Micro Letters

e-ISSN 2150-5551
CN 31-2103/TB

ARTICLE

https://doi.org/10.1007/s40820-024-01334-3

Cite as
Nano-Micro Lett.
(2024) 16:109

Received: 10 October 2023
Accepted: 11 December 2023

Discovering Cathodic Biocompatibility for Aqueous Zn–MnO_2 Battery: An Integrating Biomass Carbon Strategy

Wei Lv[1] ✉, Zilei Shen[1], Xudong Li[1], Jingwen Meng[1], Weijie Yang[2], Fang Ding[3] ✉, Xing Ju[1], Feng Ye[1], Yiming Li[4], Xuefeng Lyu[1], Miaomiao Wang[1], Yonglan Tian[1], Chao Xu[1] ✉

HIGHLIGHTS

- γ-MnO_2 loaded on N-doped biomass carbon from grapefruit peel is firstly developed.
- The splendid cathodic properties (e.g., coulombic efficiency: ~ 100%, energy density: 553.12 Wh kg^{-1}) are gained.
- The biomass strategy guaranteed via cytotoxicity test shows a clinical potential.
- Zn-ion storage efficiency is boosted mainly by regulating Mn–O bond and Mn domains.

ABSTRACT Developing high-performance aqueous Zn-ion batteries from sustainable biomass becomes increasingly vital for large-scale energy storage in the foreseeable future. Therefore, γ-MnO_2 uniformly loaded on N-doped carbon derived from grapefruit peel is successfully fabricated in this work, and particularly the composite cathode with carbon carrier quality percentage of 20 wt% delivers the specific capacity of 391.2 mAh g^{-1} at 0.1 A g^{-1}, outstanding cyclic stability of 92.17% after 3000 cycles at 5 A g^{-1}, and remarkable energy density of 553.12 Wh kg^{-1} together with superior coulombic efficiency of ~ 100%. Additionally, the cathodic biosafety is further explored specifically through in vitro cell toxicity experiments, which verifies its tremendous potential in the application of clinical medicine. Besides, Zinc ion energy storage mechanism of the cathode is mainly discussed from the aspects of Jahn–Teller effect and Mn domains distribution combined with theoretical analysis and experimental data. Thus, a novel perspective of the conversion from biomass waste to biocompatible Mn-based cathode is successfully developed.

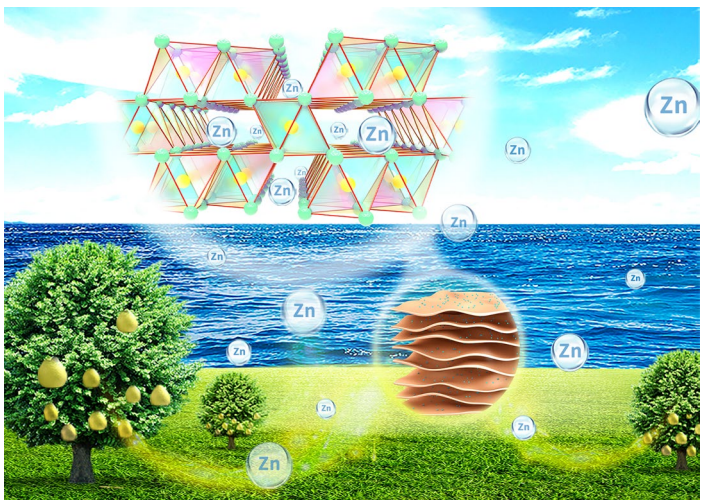

KEYWORDS Aqueous Zn-ion batteries; Biocompatibility; Jahn–Teller effect; Mn domains; γ-MnO_2

✉ Wei Lv, luidavid@126.com; Fang Ding, dingfang0707@ibp.ac.cn; Chao Xu, mechxu@ncepu.edu.cn
[1] Institute of Energy Power Innovation, North China Electric Power University, Beijing 102206, People's Republic of China
[2] Department of Power Engineering, School of Energy, Power and Mechanical Engineering, North China Electric Power University, Baoding 071003, People's Republic of China
[3] Key Laboratory of RNA Biology, Institute of Biophysics, Chinese Academy of Sciences, Beijing 100101, People's Republic of China
[4] Collaborative Innovation Center of Integrated Exploitation of Bayan Obo Multi-Metal Resources, Inner Mongolia University of Science and Technology, Baotou 014010, People's Republic of China

Published online: 05 February 2024

Shanghai Jiao Tong University Press

Springer

1 Introduction

With the continuous global carbon emission, biomass energy as a kind of green renewable, biodegradable and nontoxic energy resource has attracted considerable attention [1–8]. In other words, the recycling of biomass resources as a feasible way to achieve carbon neutrality shows tremendous potential in the field of energy [9–16], materials, health care, and so on [17–24]. In particular, the development of high safe and green large-scale energy storage technology using biomass is of great significance for building a clean and low-carbon modern energy system [25–32]. Lithium-ion batteries have been widely used in new energy electric vehicles [33–46], but the utilization of flammable organic electrolytes plus high manufacturing costs for lithium batteries are not conducive to the application in large-scale energy storage [47–57]. Therefore, the inexpensive and eco-friendly aqueous Zn-ion batteries (AZIBs) with high-safety are considered to have great potential in massive-scale energy storage [58–65]. There are many factors affecting the properties of AZIBs, among which the development of stable cathodic materials becomes the key [66–73], and thereinto, MnO_2 with the characteristics of diverse structures (α-, β-, γ-, and δ-, etc.), low price, and environmental friendliness has been widely used as cathodic materials of AZIBs [74–81]. Nevertheless, the repeated insertion/extraction of Zn^{2+} during charge–discharge process leads to the structural deformation for MnO_2 [82–88]. Meanwhile, Mn^{4+} is prone to be reduced to Mn^{3+} so as to induce the Jahn–Teller effect and lattice distortion [89, 90]. In addition, the disproportionation reaction of Mn^{3+} also promotes the dissolution of MnO_2 [91–96]. Thus, exploring sustainable and renewable biomass resources to improve the structural stability of MnO_2 would be a "Win–Win" strategy.

The recombination of carbon materials and MnO_2 has been identified as an important way to optimize the cathodic performance of aqueous Zn–MnO_2 batteries [97–99]. Chen et al. synthesized carbon nanofiber@δ-MnO_2 with a facile method combining solid-grinding and wet-chemical reaction, and achieved a capacity of 277 mAh g^{-1} and capacity retention of 79.78% after 700 cycles at 200 mA g^{-1} [100]. Li et al. prepared N-doped carbon nanowires incorporated with δ-MnO_2 by hydrothermal method, the discharge capacities of which were 325 mAh g^{-1} at 100 mA g^{-1} and 90 mAh g^{-1} at 2 A g^{-1} respectively, and its cycle life after 2500 cycles was 95% at 2 A g^{-1} [101]. Huang et al. electrochemically deposited α-MnO_2 onto carbon nanotube as cathode, which achieved the specific capacities of 292.7 and 105.6 mAh g^{-1} at 0.2 and 3 mA cm^{-2} respectively, and its cycling life remained 88.5% after 300 cycles at 0.3 mA cm^{-2} [102]. Moreover, Kim et al. reported a carbon-coated α-MnO_2 cathode, which exhibits a discharge capacity of 272 mAh g^{-1} and cycle life of 69.49% after 50 cycles at 66 mA g^{-1} [103]. Overall, carbon materials used to be compound with MnO_2 are mainly based on the conventional commercial materials such as carbon nanofiber, carbon nanotube, etc. Therefore, the research on how to improve Zn-ion storage performance by constructing Mn-based cathode compounded with carbon materials derived from biomass, especially the inexpensive and renewable biomass waste, is still rare.

In this work, the abundant grapefruit peel as a natural biomass carbon source is adopted to synthesize N-doped carbon carrier powder (CP) through a simple calcination in N_2 atmosphere, and γ-MnO_2 prepared by electro-deposition is uniformly loaded onto CP to obtain the composite cathode (γ-MnO_2@CP). A systematic study about the improving mechanism of Zn-ion storage efficiency via compounding CP is conducted from multiple perspectives of Jahn–Teller effect, Mn valence, and Mn domains, etc. Besides, the in vitro cytotoxicity experiments of pure γ-MnO_2 and γ-MnO_2@CP are carried out to investigate the application prospect in the field of biomedicine. Therefore, the above research provides a valuable guidance for the comprehensive utilization of wasted biomass to design high-performance MnO_2-biomass carbon cathode.

2 Experimental Section

2.1 Sample Preparation

The grapefruit peel was washed three times by deionized water, then heated at 80 °C for 3 h and crushed into yellow powder, which was heated at 650 °C for 2 h under a nitrogen atmosphere to obtain CP. A three-electrode system composed of a stainless steel working electrode, a saturated calomel reference electrode, and a platinum plate counter electrode was used for MnO_2 electro-deposition under the current density of 5 mA cm^{-2} for 30 min with electromagnetic stirring, and the electrolyte was made up of 0.5 M

https://doi.org/10.1007/s40820-024-01334-3

$Mn(CH_3COO)_2$ and 0.5 M Na_2SO_4, the chemical reaction occurred on the surface of stainless steel working electrode is described as: $Mn^{2+} + 2H_2O \rightarrow MnO_2 + 4H^+ + 2e^-$. Finally, the thin films of MnO_2 electrochemically deposited on the stainless steel electrode were scrapped off. The mixtures of as-prepared MnO_2 and CP (Quality percentage of CP: 10, 20, 30, and 40 wt%) were magnetically stirred in deionized water for 1 h, and then ultrasonically dispersed for another 1 h respectively, the above solutions were centrifuged and then dried at 80 °C (Heating rate: ~ 2 °C min^{-1}) in air for 3 h to obtain the cathodic active materials, which were labelled as CP-10, CP-20, CP-30 and CP-40, respectively. Besides, the as-prepared MnO_2 mentioned above was labelled as CP-0.

2.2 Materials Characterization

The X-ray diffraction (XRD) profiles were measured with Bruker-D8 Advance X-ray diffractometer (Cu Kα radiation, 2θ step: 0.02°) and analyzed with Jade 5.0 software. The spectroscopic property was tested though PerkinElmer Spectrum 100 FTIR. The micro morphology was observed through JEOL JEM-2100F TEM and Nova Nano SEM 450. The composition and valence state were tested by Thermo ESCALAB 250XI XPS.

2.3 Computational Calculation

All the theoretical calculation about the models of Zn^{2+} intercalating into the tunnel structures of pure γ-MnO_2 and γ-MnO_2@CP were performed with VASP software based on density functional theory (DFT) in this work. The migration behavior of Zn^{2+} was computed by mean square displacement (*MSD*) using the equation $MSD = \frac{1}{M}\sum_{i=1}^{M}\left|r_i(t) - r_i(0)\right|^2$, where r_i (0) is the initial position of Zn^{2+}, r_i (*t*) is the terminal position of Zn^{2+}, and *M* is the number of simulation, then the diffusion coefficient (*D*) of Zn^{2+} was calculated by fitting 6*t* to *MSD* as the Einstein relation: $D = \lim_{t\to\infty}\frac{MSD}{6t}$ [74]. The adsorption energy (E_{ads}) values of Zn^{2+} and OH^- on the tunnel structural surface of γ-MnO_2 were calculated, and the bader charges of the above two models were also simulated respectively. Meanwhile, Mn–O bond lengths of MnO_6 octahedron in the above two models were calculated for structural analysis.

2.4 Electrochemical Properties

The cathodic active materials (CP-0, CP-10, CP-20, CP-30, and CP-40), acetylene black and poly-vinylidene fluoride were mixed together in accordance with the gravimetric ratio of 7:2:1, and N-methyl-2-pyrrolidone was added into the above mixtures to produce black slurries, which were then painted on 5 stainless steel webs (Diameter: ~ 14 mm) and then heated at 80 °C (Heating rate: ~ 2 °C min^{-1}) in air for 8 h to obtain the cathodic current collectors (Load quality of active substance: ~ 2 mg cm^{-2}). A CR2032 button battery configuration with a Whatman glass-fiber diaphragm (Grade GF/D), Zn anode, and the electrolyte of 2 mol L^{-1} $ZnSO_4$ and 0.1 mol L^{-1} $MnSO_4$ was used to estimate the cathodic active materials, the prepared button batteries shared the same numbers as CP-0, CP-10, CP-20, CP-30, and CP-40 respectively. The galvanostatic charge/discharge performance was tested using LANHE CT3002A equipment (Voltage: 0.8–1.8 V) based on the active material mass. The cyclic voltammetry (CV) curves were recorded using a CHI660E electrochemical work station (Scan rate: 0.1, 0.2, 0.4, 0.6, and 0.8 mV s^{-1}), then *b* value was obtained according to the equation $\log(i) = \log(a) + b\log(v)$ (*i*: Peak current; *v*: Scan rate; *a* and *b*: Adjustable values), the pseudocapacitive fitting was calculated on the basis of the relational expression $i(V) = k_1v + k_2v^{0.5}$ (k_1v: Non-diffusion controlled contribution; $k_2v^{0.5}$: Diffusion controlled contribution).

2.5 In Vitro Cytotoxicity

3T3 mouse embryonic fibroblast cells were cultured in DMEM medium (Gibco, USA) supplemented with 10% fetal bovine serum (FBS, Gibco, USA) and 1% penicillin/streptomycin (Gibco, USA) at 37 °C. In vitro cell viability was evaluated by CCK-8 assay against 3T3 cells. Briefly, cells were seeded in 96-well plates and incubated with the as-synthesized materials, including CP-0, CP-10, CP-20, CP-30, and CP-40. 10 μL CCK-8 solution was added to each well and the absorbance was recorded on a microplate reader (EnSpire, USA) at 490 nm. Cell apoptosis assay was conducted by using an Annexin V-FITC/PI apoptosis detection kit (Beyotime, China). For apoptosis assay, 3T3 cells were seeded into 6-well plates and incubated with the above-mentioned materials for 48 h. Thereafter, cells were stained with Annexin V FITC/PI for 30 min and the apoptosis percentage

was detected by a flow cytometer (BD FACS Calibur, USA). Calcein AM/PI Co-staining was performed to detect the live/dead cells under different treatments. Following incubation cells were stained with calcein AM and PI for 30 min, and the stained cells were imaged by a fluorescence microscope (NIKON, Japan). For the above experiments, cells in PBS were set as the control group.

3 Results and Discussions

3.1 Microstructure

The preparation detail of CP is schematically illustrated in Fig. 1a, and the N-doped biomass carbon is expected to be obtained. As shown in Fig. 1b, all the samples display five characteristic peaks indexed to (120), (131), (300), (160), and (421) crystal planes, which means that γ-MnO_2 is successfully synthesized by electro-deposition corresponding to JCPDS No. 14-0644 [104], and the broad peaks at around 26° belonging to (002) crystal plane of carbon for CP-10, CP-20, CP-30, and CP-40 are also observed [100]. Compared with CP-0, a new peak at around 1025 cm^{-1} corresponding to Mn–O–C bond is observed in the FTIR spectrum of CP-20 (Fig. 1c), which once again demonstrates the successful recombination of CP and γ-MnO_2 for CP-20. The characteristic planes of CP and γ-MnO_2 are also observed in SAED pattern (Fig. 1d), and the HRTEM images of CP-20 indicate that the interplanar spacings of 0.162 and 0.241 nm are well indexed to the lattice planes of (160) and (131) for γ-MnO_2 (Fig. 1e, f), which further confirms the accuracy of the analytical result from Fig. 1b, d. Figure 1g shows a successful loading of γ-MnO_2 nanoparticles on the surface of irregular flower-like CP. The EDS result shows a uniform element distribution of Mn, O, C, and N for CP-20 (Fig. 1h–k), and the XPS result once again affirms the coexistence of Mn, O, C, and N on the surface of CP-20 (Fig. 1l–o). Besides, Fig. S1 certifies the existence of Mn and O elements for CP-0, and Figs. S2, S3, and S4 also reveal the existence of Mn, O, C, and N elements for CP-10, CP-30, and CP-40 respectively, meanwhile the coexistence of Mn^{3+} and Mn^{4+} is revealed for all the samples.

The Jahn–Teller effect primarily due to high-spin Mn^{3+} with $(t_{2g})^3(e_g)^1$ electron configuration in 3*d* orbital usually leads to detrimental structural disorder for MnO_2, so MnO_2 with a higher Mn valence is promising to exhibit excellent long-term cycling stability [105]. Therefore, the compound strategy of γ-MnO_2 with CP is beneficial to reduce the content of Mn^{3+}, and it's worth noting that CP-20 exhibits the highest percent of Mn^{4+} (93.68%) and the lowest percent of Mn^{3+} (6.32%), which foreshadows the weakest Jahn–Teller effect in CP-20 (Figs. 1l and S1a, S2a, S3a, S4a).

3.2 Theoretical Calculation

As shown in Fig. 2a, the calculated *D* values of Zn^{2+} in the internal structures of pure γ-MnO_2 and γ-MnO_2@CP are 70×10^{-6} and 174×10^{-6} $Å^2$ fs^{-1} respectively, and it can be seen that the CP composite strategy effectively improves Zn^{2+} kinetics. The E_{ads} values of Zn^{2+} on the tunnel-shaped surface of pure γ-MnO_2 and γ-MnO_2@CP are −2.968 and −2.353 eV respectively, which demonstrates that Zn^{2+} is more liable to migrate smoothly inside γ-MnO_2@CP (Fig. 2b). Bader charge (1.11*e*) of Zn^{2+} and γ-MnO_2@CP group is less than that (1.323*e*) of Zn^{2+} and pure γ-MnO_2 group, and this implies a more obvious electron transfer tendency and a stronger binding interaction between Zn^{2+} and pure γ-MnO_2, which hinders the diffusion of Zn^{2+} (Fig. 2c). Besides, the nano-sized Mn-based cathode effectively reduces the migration time of Zn^{2+} according to the equation $\tau_{eq}=L^2/2D$ (τ_{eq}: Diffusion time; *L*: Material size; *D*: Diffusion coefficient) [69], so the combination of nanocrystallization for γ-MnO_2 (Fig. 1g) and CP composite strategy would be helpful to boost Zn storage efficiency theoretically.

3.3 Electrochemical Property

It is worth noting that the cathodic peaks shift toward higher values and the anodic peaks shift toward lower values for CP-10, CP-20, CP-30, and CP-40 compared with those of CP-0 from the CV curves at 0.4 mV s^{-1}, which indicates the reduced inherent voltage polarization plausibly related to CP composite, and especially the smallest polarization is seen in CP-20, and CP-20 also shows the highest peak current density implying its largest electrochemical capacity (Fig. 3a). CP-20 with a medium potential of ~1.4 V displays a maximum discharge capacity of 391.2 mA g^{-1} and a minimum voltage hysteresis when the current density is 0.1 A g^{-1} among the samples (Fig. 3b). The high rate discharge ability of γ-MnO_2 mixed with CP are better

 https://doi.org/10.1007/s40820-024-01334-3

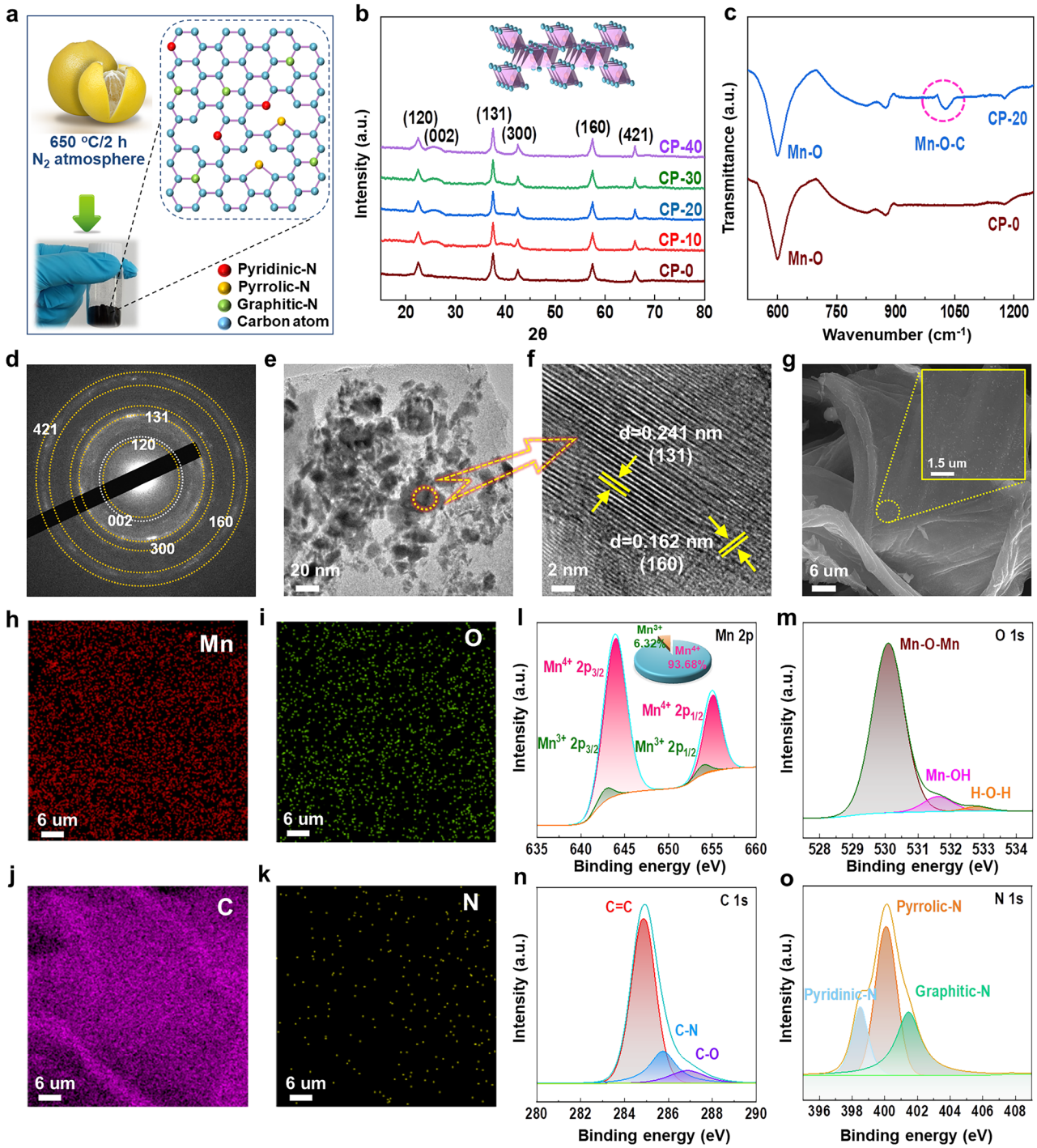

Fig. 1 **a** Schematic diagram for the preparation of CP. **b** XRD patterns of CP-0, CP-10, CP-20, CP-30, and CP-40. **c** FTIR spectra of CP-0 and CP-20. **d** SAED, **e** and **f** HRTEM, **g** SEM, **h–k** EDS of CP-20. XPS high-resolution patterns of **l** Mn 2*p*, **m** O 1*s*, **n** C 1*s*, and **o** N 1*s* of CP-20.

than that of pure γ-MnO_2 when the current density increases from 0.1 to 5 A g^{-1} and then reduces to 0.1 A g^{-1}, besides CP-20 also exhibits the optimal discharge capability of 189.8 mAh g^{-1} at 5 A g^{-1} compared with other samples (Fig. 3c). The cyclic stability of CP-0 is only 24.54% after 200 cycling times at 0.1 A g^{-1}, while CP-20 demonstrates the best cycling performance (89.47%) and coulombic efficiency (~ 100%) (Fig. 3d). In particular, the 3000 times cycling life of CP-20 achieves even high up to 92.17%, and its coulombic efficiency still maintains at ~ 100% at 5 A g^{-1} (Fig. 3e). Furthermore, the specific energy density of CP-20 at 0.1 A g^{-1} reaches 553.12 Wh kg^{-1}, which is superior to that of CP-0 (250.32 Wh kg^{-1}), CP-10 (383.08 Wh kg^{-1}), CP-30 (427.00 Wh kg^{-1}) and CP-40 (307.21 Wh kg^{-1}).

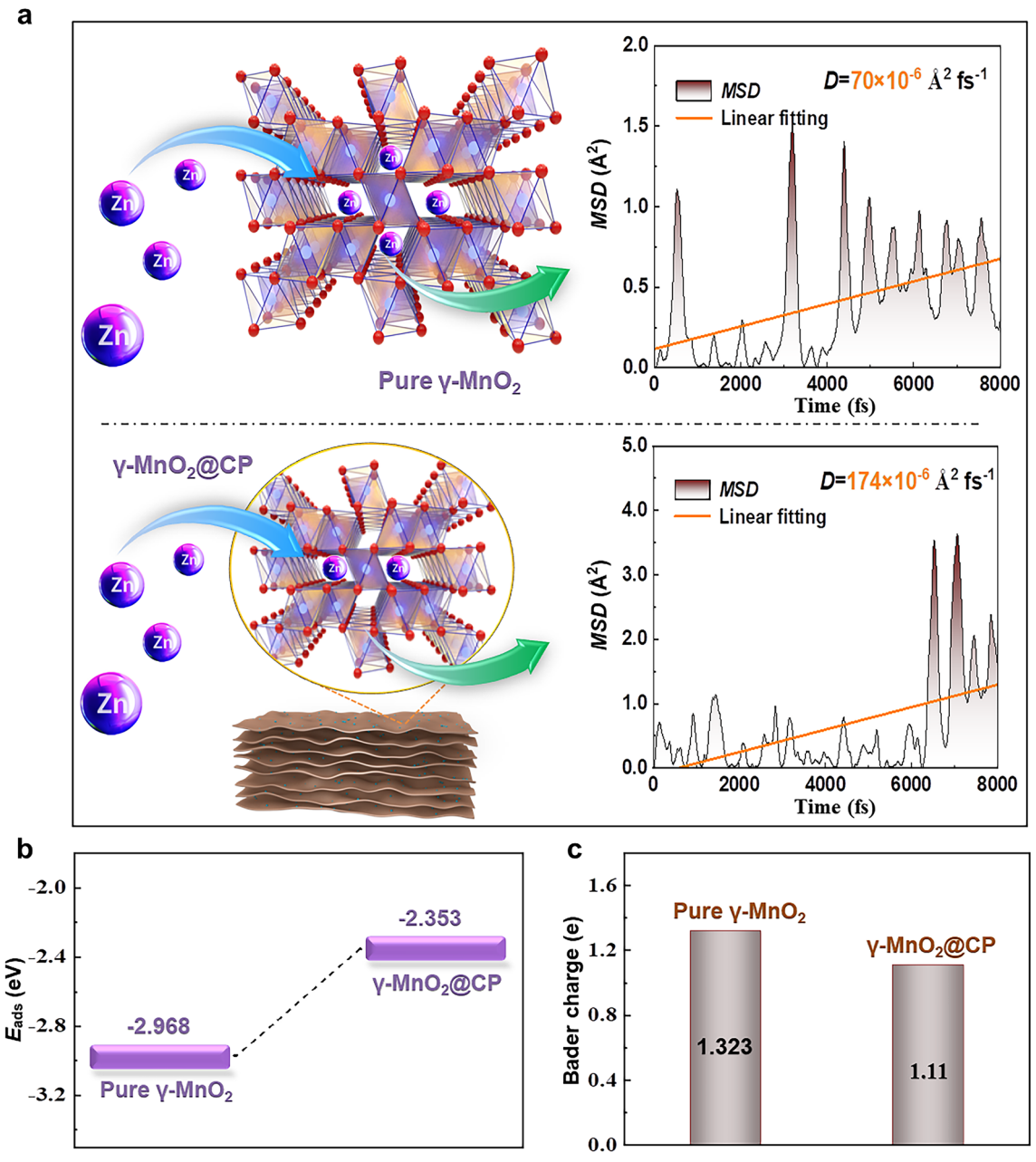

Fig. 2 Theoretical calculated results of **a** *MSD*, **b** E_{ads}, and **c** bader charge about the models of Zn^{2+} intercalating into the tunnel structures of pure γ-MnO_2 and γ-MnO_2@CP

https://doi.org/10.1007/s40820-024-01334-3

More importantly, the energy density of CP-20 in our work is also superior to those reported in literatures (Fig. 3f). To sum up, the recombination strategy with CP is of benefit to the electrochemical performance enhancement for γ-MnO_2.

As shown in Figs. S5a, S6a, S7a, S8a, and S9a, the phenomenon that the cathodic and anodic peaks of CV curves for all the samples shift toward negative and positive potentials respectively as the scan rate increases reveals a distinct insertion/deinsertion energy storage behavior of Zn^{2+} [74]. The CP-20 sample, by contrast, has a stronger redox peak and smaller gap between cathodic and anodic peak, which indicates that CP-20 is promising to have faster dynamics, less polarization and better long cycle performance among the samples. The calculated pseudocapacitive proportion results (Figs. S5b, S6b, S7b, S8b, and S9b) show that CP-20 exhibits the maximum pseudocapacitance contribution, and it is again verified that the reinforced pseudocapacitance behavior by CP composite strategy is beneficial to ameliorate the electrochemical characteristics of γ-MnO_2. Usually, a larger *b*-value (close to 1.0) is deemed to be advantageous for strengthening pseudocapacitance behavior so as to improve energy storage dynamics, obviously *b*-value of CP-20 is lager than that of other samples according to Figs. S5c, S6c, S7c, S8c, and S9c, and this also reveals the effectively promoted pseudocapacitance behaviour of CP-20. Furthermore, The fact that the peak1 and peak2 offset values of CP-20 are the smallest demonstrates again its enhanced intercalation pseudocapacitance (Figs. S5d, S6d, S7d, S8d, and S9d), which strongly supports the above fitting conclusions about pseudocapacitive and *b*-value. More significantly, the presence of pyridinic-N and pyrrolic-N is considered to be responsible for boosting the pseudocapacitance behavior of electrode materials [106], and this might be another key factor to improve the pseudocapacitance characteristics of γ-MnO_2 via CP composite. (Figs. 1o and S2d, S3d, S4d).

3.4 Mechanism Analysis

Under the current density of 0.1 A g^{-1}, the by-product $Zn_4SO_4(OH)_6{\cdot}4H_2O$ (JCPDS No. 44-0673) emerges at the fully discharged (F-D) state and almost completely fades away at the fully charged (F–C) state on the 10th cycle for CP-20, and the reversible reaction is represented by the following equation: $\gamma - MnO_2 + SO_4^{2-} + 4Zn^{2+} + 2OH^- + 6H_2O + 2e^- \leftrightarrow Mn^{2+} + Zn_4SO_4(OH)_6 \cdot 4H_2O$, while $Zn_4SO_4(OH)_6{\cdot}4H_2O$ always exists at F–D and F–C states for CP-0 (Fig. 4a). Noticeably, the calculated E_{ads} values of OH^- with the surfaces of pure γ-MnO_2 and γ-MnO_2@CP are − 3.166 and − 1.568 eV respectively (Fig. 4b), this obvious difference illustrates that OH^- is more liable to be adsorbed on the surface of pure γ-MnO_2 to promote the formation of $Zn_4SO_4(OH)_6{\cdot}4H_2O$, which reconfirms the conclusion from Fig. 4a. Herein, the CP composite strategy effectively inhibits the side effect and ultimately increases the reversibility and efficiency of Zn-ion energy storage.

The O 1*s* XPS spectra of CP-0 and CP-20 are fitted into tetravalent Mn–O–Mn bonds, trivalent Mn–OH bonds, and H–O–H bonds for residual water, correspondingly the average Mn valences of CP-0/CP-20 are estimated to be 3.6 +/3.8 + at F–D state and 3.75 +/3.95 + at F–C state on the 10th cycle according to the area contributions of Mn–O–Mn and Mn–OH components respectively (Fig. 4c). More precisely, the average oxidation state (AOS) of Mn can be computed based on the equation AOS = 8.95–1.13 ΔE_{Mn3s}, where ΔE_{Mn3s} is the energy difference between the main and satellite peaks in Mn 3*s* XPS spectra [107], so the AOS of Mn in CP-0 (F–D), CP-0 (F–C), CP-20 (F–D), and CP-20 (F–C) on the 10th cycle are also 3.6 +, 3.75 +, 3.8 +, and 3.95 + respectively (Fig. 4d), thus the calculated Mn valence from Mn 3*s* and O 1*s* XPS spectra are entirely the same, which further illustrates that the CP composite is beneficial to suppress the Jahn–Teller effect by regulating Mn valence, besides the Zn 3*p* peak of CP-0 is also lower than that of CP-20. Meanwhile, the Zn 2*p* peaks of CP-20 are apparently stronger than that of CP-0 on the 10th cycle at F-D state (Fig. 4e), which reconfirms the conclusion in Fig. 4d. Different from the Mn–O bonds of γ-MnO_2@CP nearly without distortion, the Jahn–Teller effect induces a geometric distortion with two longer (O5 and O6) Mn–O bonds of pure γ-MnO_2 according to theoretical calculation (Fig. 4f). The formation of Mn domains is supposed to disrupt the cooperativity of Jahn–Teller effect as schematically shown in Fig. 4g [108], and the Mn domains with different orientation are also visually identified in CP-20 (Fig. 4h) but not in CP-0 (Fig. 4i), hence the CP composite strategy promotes the anisotropic Jahn–Teller distortion to improve the structural stability of γ-MnO_2.

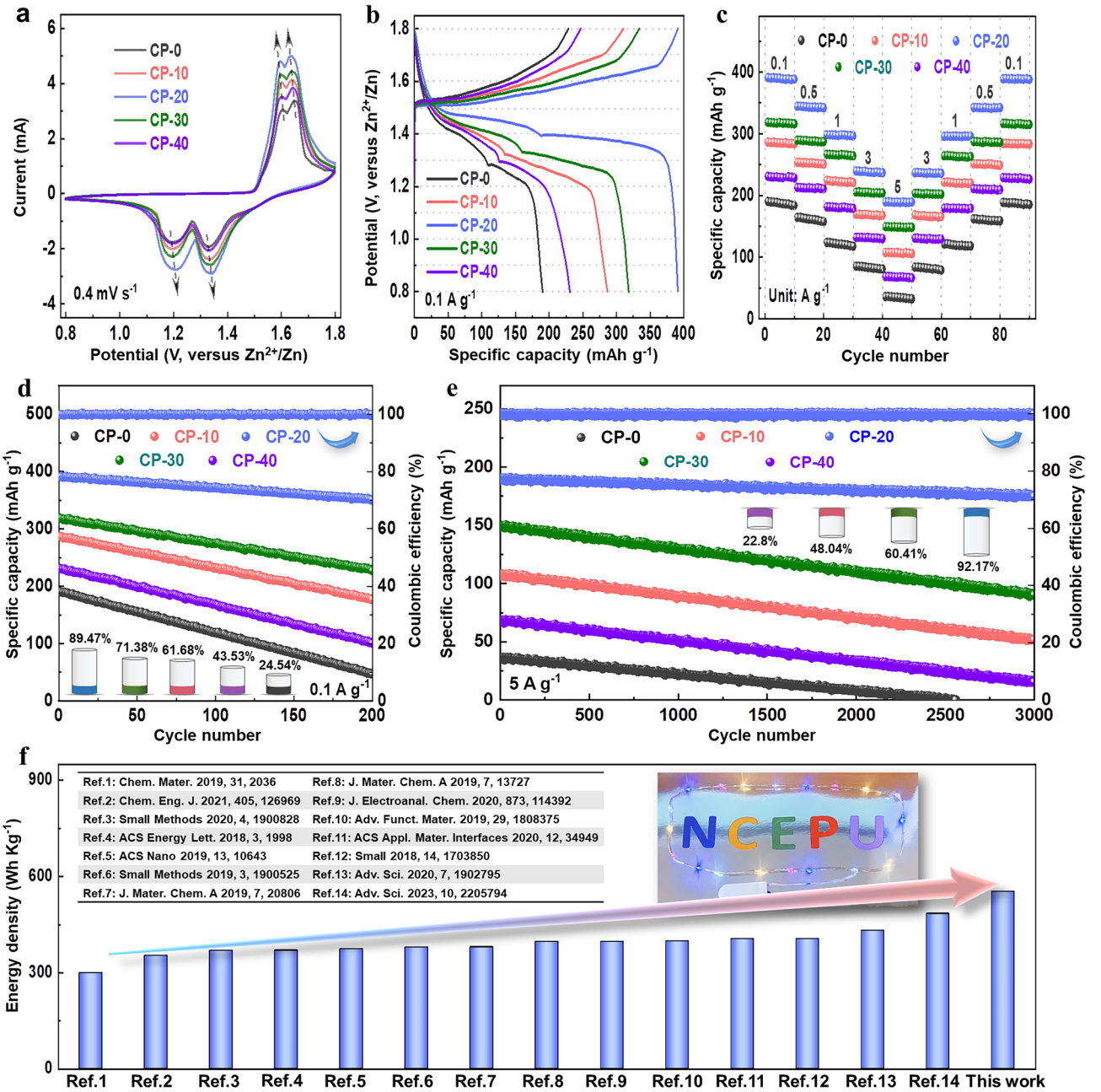

Fig. 3 Electrochemical test results of **a** CV curves, **b** constant current charge–discharge profiles, **c** high rate discharge ability, **d** 200 times cycling performance, and **e** 3000 times cyclic stability of CP-0, CP-10, CP-20, CP-30, and CP-40. **f** Comparison diagram about the energy density calculated based on cathodic active material mass between literatures and CP-20

3.5 In Vitro Cell Toxicity

To investigate the intrinsic cytotoxicity of the above-mentioned samples against 3T3 cell, CCK-8 assay is performed to determine the relative cell viability after 24, 48, and 72 h of incubation, respectively. Currently, cells treated with PBS are set as a reference. Negligible proliferation inhibition is observed in cells with the treatment of CP-10, CP-20, CP-30, and CP-40 even up to 72 h of incubation compared with the control group, while exposure to CP-0 exhibits notable cytotoxicity to cells as the relative cell viability decreases over 50% after 72 h (Fig. 5a), indicating the desirable

https://doi.org/10.1007/s40820-024-01334-3

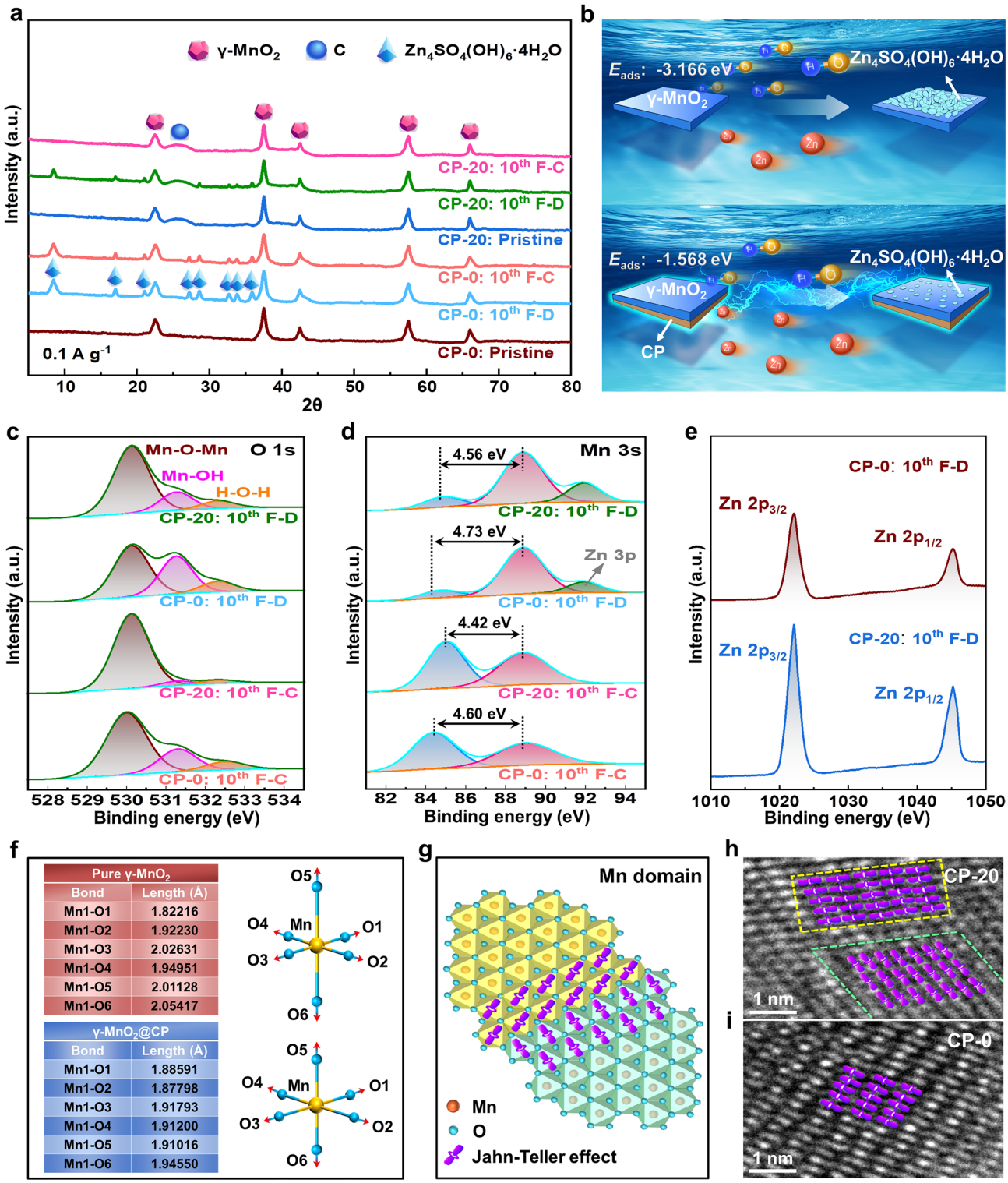

Fig. 4 **a** Ex-situ XRD of CP-0 and CP-20 at F-D/F–C states on the 10th cycle. **b** Sketch map at F-D state and the calculated E_{ads} values of OH^- to the surface of γ-MnO_2. XPS high-resolution patterns of **c** O 1*s*, **d** Mn 3*s* and **e** Zn 2*p* of CP-0 and CP-20. **f** Calculated Mn–O bonding distances of MnO_6 octahedra of pure γ-MnO_2 and γ-MnO_2@CP. **g** Schematic Mn domains and **h**, **i** actually observed Mn domains

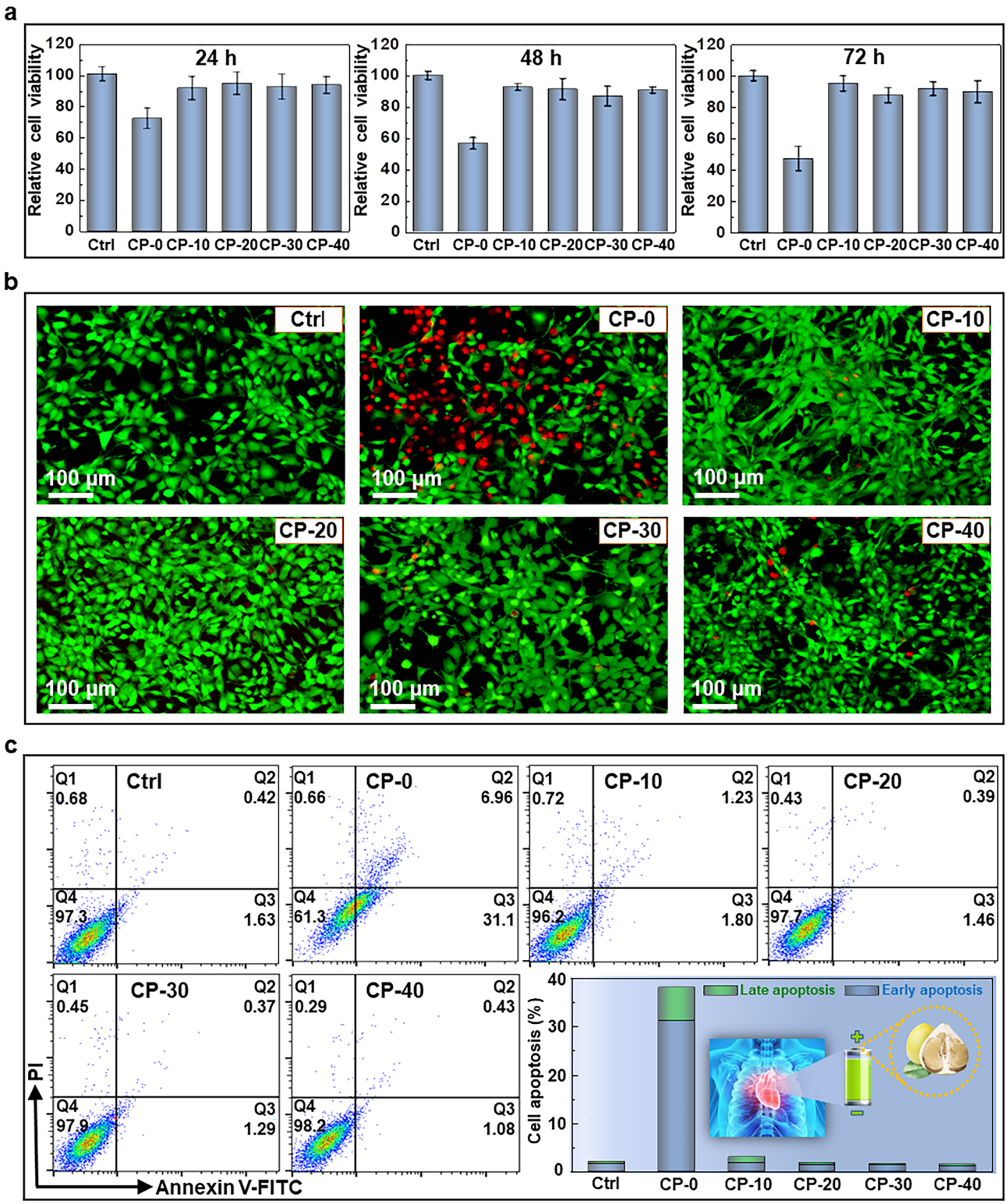

Fig. 5 **a** Relative cell viability of 3T3 cells at different time points post treatment. **b** Fluorescence microscopic images of 3T3 cells by Calcein AM/PI staining at 48 h with various treatments. **c** Cell apoptosis percentage of 3T3 cells upon different treatments for 48 h by flow cytometry (Ctrl: cells treated with PBS)

https://doi.org/10.1007/s40820-024-01334-3

biocompatibility of the above samples except CP-0. Besides, Calcein AM/PI staining is carried out to assess the live/dead cell after different treatments, and no evident cell death is noticed in cells under these above treatments other than CP-0 as expected (Fig. 5b), which is consistent with the results of CCK-8 assay. Furthermore, flow cytometry is performed to investigate the apoptosis profile of 3T3 cells incubated with each sample for 48 h, and no apoptosis is induced by most of the as-synthesized materials with a total apoptotic cell rate less than 5% compared to the control group, but exposure to CP-0 results in severe cell apoptosis as indicated by nearly 40% of total apoptosis percentage (Fig. 5c), and it is in good accordance with the cell toxicity results. It is verified that CP-10, CP-20, CP-30, and CP-40 possess better biosafety compared with CP-0, which might be attributed to the loading of biocompatible CP. Therefore, the CP composite strategy shows a great potential not only in the field of large-scale energy storage, but also in clinical applications.

4 Conclusion

The environmental friendly AZIBs with considerable theoretical capacity (820 mAh g^{-1}) and appropriate redox potential (−0.763 V versus standard hydrogen electrode) attract researchers' broad concern recently [109–117]. Thereinto, biocompatible AZIBs are proposed as candidates for powering biocompatible electronics due to their excellent features of low cost, high-level safety and high-performance [118–120]. Hence, the biomass CP derived from waste grapefruit peel is successfully prepared, and the electrochemical properties and biocompatibility for the composite cathode of γ-MnO_2 loaded on CP are simultaneously investigated in the present work. The considerable electrochemical properties of 3000 times long cycle stability at 5 A g^{-1} (92.17%), energy density (553.12 Wh kg^{-1}), and coulombic efficiency (~100%) for the composite cathode with CP quality percentage of 20 wt% are achieved, which is mainly ascribed to the effective regulation of Mn–O bond distance, Mn valence, and Mn domains combined with experimental and DFT computational analysis. Furthermore, the cathodic biosafety is also verified via in vitro test extensively. In brief, this work not only brings forward a feasible countermeasure for structural regulation of multi-function Mn-based cathode with inexpensive biomass-derived carbon, but also paves a novel way for the application of AZIBs in biomedical field.

Acknowledgements This work was supported by the National Natural Science Foundation of China [Grant no. 51821004].

Declarations

Conflict of Interest The authors declare no interest confict. Twests or personal relationships that could have appeared to influence the work reported in this paper.

Supplementary Information The online version contains supplementary material available at https://doi.org/10.1007/s40820-024-01334-3.

References

1. J. Zeng, L. Bi, Y. Cheng, B. Xu, A.K.-Y. Jen, Self-assembled monolayer enabling improved buried interfaces in blade-coated perovskite solar cells for high efficiency and stability. Nano Res. Energy **1**, e9120004 (2022). https://doi.org/10.26599/nre.2022.9120004
2. Z. Li, J. Fu, X. Guo, How to commercialize solid-state batteries: a perspective from solid electrolytes. Natl. Sci. Open **2**, 20220036 (2023). https://doi.org/10.1360/nso/20220036
3. X. Xuan, M. Qian, L. Pan, T. Lu, Y. Gao et al., A hollow tubular NiCo layacknered double hydroxide@Ag nanowire structure for high-power-density flexible aqueous Ni//Zn battery. J. Energy Chem. **70**, 593–603 (2022). https://doi.org/10.1016/j.jechem.2021.12.013
4. G.-Y. Wang, X.-H. Wang, J.-F. Sun, Y.-M. Zhang, L.-R. Hou et al., Porous carbon nanofibers derived from low-softening-point coal pitch towards all-carbon potassium ion hybrid capacitors. Rare Met. **41**, 3706–3716 (2022). https://doi.org/10.1007/s12598-022-02067-1
5. W. Li, P. Luo, Z. Fu, X. Yuan, M. Huang et al., Highly reversible and stable manganese (II/III)-centered polyoxometalates for neutral aqueous redox flow battery. Next Energy **1**, 100028 (2023). https://doi.org/10.1016/j.nxener.2023.100028
6. A. Hao, X. Wan, X. Liu, R. Yu, J. Shui, Inorganic microporous membranes for hydrogen separation: challenges and

solutions. Nano Res. Energy **1**, e9120013 (2022). https://doi.org/10.26599/nre.2022.9120013

7. K. Wu, F. Ning, J. Yi, X. Liu, J. Qin et al., Host-guest supramolecular interaction behavior at the interface between anode and electrolyte for long life Zn anode. J. Energy Chem. **69**, 237–243 (2022). https://doi.org/10.1016/j.jechem.2022.01.037
8. H.-J. Liang, X.-T. Li, W.-Z. Zheng, Z.-T. Liu, W. Yang et al., Rational design of heterostructured core–shell Co-Zn bimetallic selenides for improved sodium-ion storage. Rare Met. **41**, 3381–3390 (2022). https://doi.org/10.1007/s12598-022-02035-9
9. X. Fang, L. Zeng, Z. Li, L.A. Robertson, I.A. Shkrob et al., A cooperative degradation pathway for organic phenoxazine catholytes in aqueous redox flow batteries. Next Energy **1**, 100008 (2023). https://doi.org/10.1016/j.nxener.2023.100008
10. S. Wang, J. Ma, X. Shi, Y. Zhu, Z.-S. Wu, Recent status and future perspectives of ultracompact and customizable microsupercapacitors. Nano Res. Energy **1**, e9120018 (2022). https://doi.org/10.26599/nre.2022.9120018
11. C. Mao, Y. Chang, X. Zhao, X. Dong, Y. Geng et al., Functional carbon materials for high-performance Zn metal anodes. J. Energy Chem. **75**, 135–153 (2022). https://doi.org/10.1016/j.jechem.2022.07.034
12. Y. Chai, X. Xie, Z. He, G. Guo, P. Wang et al., A smelting-rolling strategy for ZnIn bulk phase alloy anodes. Chem. Sci. **13**, 11656–11665 (2022). https://doi.org/10.1039/d2sc04385h
13. T. Gao, G. Yan, X. Yang, Q. Yan, Y. Tian et al., Wet spinning of fiber-shaped flexible Zn-ion batteries toward wearable energy storage. J. Energy Chem. **71**, 192–200 (2022). https://doi.org/10.1016/j.jechem.2022.02.040
14. C. Hou, G. Tai, Y. Liu, Z. Wu, X. Liang et al., Borophene-based materials for energy, sensors and information storage applications. Nano Res. Energy **2**, e9120051 (2023). https://doi.org/10.26599/nre.2023.9120051
15. F. Tao, Y. Liu, X. Ren, J. Wang, Y. Zhou et al., Different surface modification methods and coating materials of zinc metal anode. J. Energy Chem. **66**, 397–412 (2022). https://doi.org/10.1016/j.jechem.2021.08.022
16. Y.-D. Guo, J.-C. Jiang, J. Xie, X. Wang, J.-Z. Li et al., Enhanced performance of core–shell structured sodium manganese hexacyanoferrate achieved by self-limiting Na^+–Cs^+ ion exchange for sodium-ion batteries. Rare Met. **41**, 3740–3751 (2022). https://doi.org/10.1007/s12598-022-02068-0
17. J. Xu, Z. Peng, Redox chemistry in solid catalysts for regulating oxygen electrode working mechanism in aqueous electrolytes, what's next? Next Mater. **1**, 100006 (2023). https://doi.org/10.1016/j.nxmate.2023.100006
18. L. Meng, L. Li, Recent research progress on operational stability of metal oxide/sulfide photoanodes in photoelectrochemical cells. Nano Res. Energy **1**, e9120020 (2022). https://doi.org/10.26599/nre.2022.9120020
19. X. Tong, Y. Li, N. Pang, Y. Zhou, D. Wu et al., Highly active cobalt-doped nickel sulfide porous nanocones for high-performance quasi-solid-state zinc-ion batteries. J. Energy Chem. **66**, 237–249 (2022). https://doi.org/10.1016/j.jechem.2021.08.020
20. Y. Zhang, L. Zhao, Y. Liang, X. Wang, Y. Yao, Effect of electrolyte anions on the cycle life of a polymer electrode in aqueous batteries. eScience **2**, 110–115 (2022). https://doi.org/10.1016/j.esci.2022.01.002
21. X. Guo, H. Sun, C. Li, S. Zhang, Z. Li et al., Defect-engineered Mn_3O_4/CNTs composites enhancing reaction kinetics for zinc-ions storage performance. J. Energy Chem. **68**, 538–547 (2022). https://doi.org/10.1016/j.jechem.2021.12.033
22. L. Chu, S. Zhai, W. Ahmad, J. Zhang, Y. Zang et al., High-performance large-area perovskite photovoltaic modules. Nano Res. Energy **1**, e9120024 (2022). https://doi.org/10.26599/nre.2022.9120024
23. H. Jiang, W. Gong, Y. Zhang, X. Liu, M. Waqar et al., Quench-tailored Al-doped V_2O_5 nanomaterials for efficient aqueous zinc-ion batteries. J. Energy Chem. **70**, 52–58 (2022). https://doi.org/10.1016/j.jechem.2022.02.030
24. Y. Liu, S. Liu, X. Xie, Z. Li, P. Wang et al., A functionalized separator enables dendrite-free Zn anode via metal-polydopamine coordination chemistry. InfoMat **5**, e12374 (2023). https://doi.org/10.1002/inf2.12374
25. J. Liu, J. Xiao, J. Yang, W. Wang, Y. Shao et al., The TWh challenge: next generation batteries for energy storage and electric vehicles. Next Energy **1**, 100015 (2023). https://doi.org/10.1016/j.nxener.2023.100015
26. J. Yan, F. Ye, Q. Dai, X. Ma, Z. Fang et al., Recent progress in carbon-based electrochemical catalysts: from structure design to potential applications. Nano Res. Energy **2**, e9120047 (2023). https://doi.org/10.26599/nre.2023.9120047
27. M. Chen, W. Zhou, Q. Tian, X. Han, Y. Tan et al., Artificial solid electrolyte interface layer based on sodium titanate hollow microspheres assembled by nanotubes to stabilize zinc metal electrodes. J. Energy Chem. **71**, 539–546 (2022). https://doi.org/10.1016/j.jechem.2022.03.026
28. J.-Y. Xie, K. Wang, N.-N. Li, G.-L. Lei, H.-S. Mei et al., Rational design of integrative CNTs@Ge nanotube films as binder-free electrodes for potassium storage. Rare Met. **41**, 3107–3116 (2022). https://doi.org/10.1007/s12598-022-01998-z
29. Q. Lu, X. Zou, Y. Bu, L. An, Y. Wang et al., What matters in engineering next-generation rechargeable Zn-air batteries? Next Energy **1**, 100025 (2023). https://doi.org/10.1016/j.nxener.2023.100025
30. H. Xue, H. Gong, Y. Yamauchi, T. Sasaki, R. Ma, Photo-enhanced rechargeable high-energy-density metal batteries for solar energy conversion and storage. Nano Res. Energy **1**, e9120007 (2022). https://doi.org/10.26599/nre.2022.9120007
31. S. Gao, P. Ju, Z. Liu, L. Zhai, W. Liu et al., Electrochemically induced phase transition in a nanoflower vanadium tetrasulfide cathode for high-performance zinc-ion batteries. J. Energy Chem. **69**, 356–362 (2022). https://doi.org/10.1016/j.jechem.2022.01.003
32. Z.-H. Su, R.-H. Wang, J.-H. Huang, R. Sun, Z.-X. Qin et al., Silver vanadate ($Ag_{0.33}V_2O_5$) nanorods from Ag intercalated

 https://doi.org/10.1007/s40820-024-01334-3

vanadium pentoxide for superior cathode of aqueous zinc-ion batteries. Rare Met. **41**, 2844–2852 (2022). https://doi.org/10.1007/s12598-022-02026-w

33. W. Qiu, Y. Tian, Z. Lin, S. Lin, Z. Geng et al., High rate and ultralong life flexible all-solid-state zinc ion battery based on electron density modulated $NiCo_2O_4$ nanosheets. J. Energy Chem. **70**, 283–291 (2022). https://doi.org/10.1016/j.jechem.2022.02.012
34. J. Gu, Y. Peng, T. Zhou, J. Ma, H. Pang et al., Porphyrin-based framework materials for energy conversion. Nano Res. Energy **1**, e9120009 (2022). https://doi.org/10.26599/nre.2022.9120009
35. Y. Zhang, Y. Liu, Z. Liu, X. Wu, Y. Wen et al., MnO_2 cathode materials with the improved stability via nitrogen doping for aqueous zinc-ion batteries. J. Energy Chem. **64**, 23–32 (2022). https://doi.org/10.1016/j.jechem.2021.04.046
36. J. Lv, B. Wang, J. Hao, H. Ding, L. Fan et al., Single-crystalline Mn-based oxide as a high-rate and long-life cathode material for potassium-ion battery. eScience **3**, 100081 (2023). https://doi.org/10.1016/j.esci.2022.10.007
37. S. Wang, W. Ma, Z. Sang, F. Hou, W. Si et al., Dual-modification of manganese oxide by heterostructure and cation pre-intercalation for high-rate and stable zinc-ion storage. J. Energy Chem. **67**, 82–91 (2022). https://doi.org/10.1016/j.jechem.2021.09.042
38. K. Zhang, X. Liang, L. Wang, K. Sun, Y. Wang et al., Status and perspectives of key materials for PEM electrolyzer. Nano Res. Energy **1**, e9120032 (2022). https://doi.org/10.26599/nre.2022.9120032
39. M. Yang, Y. Wang, Z. Sun, H. Mi, S. Sun et al., Anti-aggregation growth and hierarchical porous carbon encapsulation enables the $C@VO_2$ cathode with superior storage capability for aqueous zinc-ion batteries. J. Energy Chem. **67**, 645–654 (2022). https://doi.org/10.1016/j.jechem.2021.10.025
40. D.-L. Ba, W.-H. Zhu, Y.-Y. Li, J.-P. Liu, Synergistically enhancing cycleability and rate performance of sodium titanate nanowire anode via hydrogenation and carbon coating for advanced sodium ion batteries. Rare Met. **41**, 4075–4085 (2022). https://doi.org/10.1007/s12598-022-02082-2
41. N. Wang, Z. Wu, Y. Long, D. Chen, C. Geng et al., MXene-assisted polymer coating from aqueous monomer solution towards dendrite-free zinc anodes. J. Energy Chem. **73**, 277–284 (2022). https://doi.org/10.1016/j.jechem.2022.06.009
42. Z. Wei, J. Wang, S. Guo, S.C. Tan, Towards highly salt-rejecting solar interfacial evaporation: Photothermal materials selection, structural designs, and energy management. Nano Res. Energy **1**, e9120014 (2022). https://doi.org/10.26599/nre.2022.9120014
43. H. Hong, L. Jiang, H. Tu, J. Hu, K.-S. Moon et al., Rational design and evaluation of UV curable nano-silver ink applied in highly conductive textile-based electrodes and flexible silver-zinc batteries. J. Mater. Sci. Technol. **101**, 294–307 (2022). https://doi.org/10.1016/j.jmst.2021.04.061
44. F. Yuan, Y.-C. Shao, B. Wang, Y.-S. Wu, D. Zhang et al., Recent progress in application of cobalt-based compounds as anode materials for high-performance potassium-ion batteries. Rare Met. **41**, 3301–3321 (2022). https://doi.org/10.1007/s12598-022-02052-8
45. S. Zhu, Y. Dai, J. Li, C. Ye, W. Zhou et al., Cathodic Zn underpotential deposition: an evitable degradation mechanism in aqueous zinc-ion batteries. Sci. Bull. **67**, 1882–1889 (2022). https://doi.org/10.1016/j.scib.2022.08.023
46. B. Li, Z. Li, X. Wu, Z. Zhu, Interface functionalization in inverted perovskite solar cells: from material perspective. Nano Res. Energy **1**, e9120011 (2022). https://doi.org/10.26599/nre.2022.9120011
47. X. Li, S. Zhao, G. Qu, X. Wang, P. Hou et al., Defect engineering in Co-doped Ni_3S_2 nanosheets as cathode for high-performance aqueous zinc ion battery. J. Mater. Sci. Technol. **118**, 190–198 (2022). https://doi.org/10.1016/j.jmst.2021.12.027
48. Y.-H. Du, X.-Y. Liu, X.-Y. Wang, J.-C. Sun, Q.-Q. Lu et al., Freestanding strontium vanadate/carbon nanotube films for long-life aqueous zinc-ion batteries. Rare Met. **41**, 415–424 (2022). https://doi.org/10.1007/s12598-021-01777-2
49. S.-B. Wang, Q. Ran, W.-B. Wan, H. Shi, S.-P. Zeng et al., Ultrahigh-energy and-power aqueous rechargeable zinc-ion microbatteries based on highly cation-compatible vanadium oxides. J. Mater. Sci. Technol. **120**, 159–166 (2022). https://doi.org/10.1016/j.jmst.2022.01.007
50. S. Payandeh, F. Strauss, A. Mazilkin, A. Kondrakov, T. Brezesinski, Tailoring the $LiNbO_3$ coating of Ni-rich cathode materials for stable and high-performance all-solid-state batteries. Nano Res. Energy **1**, e9120016 (2022). https://doi.org/10.26599/nre.2022.9120016
51. S. Gao, X. Zhao, Q. Fu, T. Zhang, J. Zhu et al., Highly transmitted silver nanowires-SWCNTs conductive flexible film by nested density structure and aluminum-doped zinc oxide capping layer for flexible amorphous silicon solar cells. J. Mater. Sci. Technol. **126**, 152–160 (2022). https://doi.org/10.1016/j.jmst.2022.03.012
52. X.-J. Dai, X.-X. Niu, W.-Q. Fu, D. Zheng, W.-X. Liu et al., Bismuth-based materials for rechargeable aqueous batteries and water desalination. Rare Met. **41**, 287–303 (2022). https://doi.org/10.1007/s12598-021-01853-7
53. B. Zhang, L. Qin, Y. Fang, Y. Chai, X. Xie et al., Tuning Zn^{2+} coordination tunnel by hierarchical gel electrolyte for dendrite-free zinc anode. Sci. Bull. **67**, 955–962 (2022). https://doi.org/10.1016/j.scib.2022.01.027
54. J. Liang, Q. Liu, A. Ali Alshehri, X. Sun, Recent advances in nanostructured heterogeneous catalysts for N-cycle electrocatalysis. Nano Res Energy **1**, e9120010 (2022). https://doi.org/10.2599/nre.2022.9120010
55. L. Zhang, S. Yang, W. Fu, Y. Cui, J. Wang et al., Plasma-induced ε-MnO_2 based aqueous zinc-ion batteries and their dissolution-deposition mechanism. J. Mater. Sci. Technol. **127**, 206–213 (2022). https://doi.org/10.1016/j.jmst.2022.03.028
56. X. Wu, X. Feng, J. Yuan, X. Yang, H. Shu et al., Thiophene functionalized porphyrin complexes as novel bipolar organic cathodes with high energy density and long cycle life. Energy

Storage Mater. **46**, 252–258 (2022). https://doi.org/10.1016/j.ensm.2022.01.020

57. J. Wang, B. Zhang, Z. Cai, R. Zhan, W. Wang et al., Stable interphase chemistry of textured Zn anode for rechargeable aqueous batteries. Sci. Bull. **67**, 716–724 (2022). https://doi.org/10.1016/j.scib.2022.01.010
58. J. Cao, D. Zhang, R. Chanajaree, Y. Yue, Z. Zeng et al., Stabilizing zinc anode via a chelation and desolvation electrolyte additive. Adv. Powder Mater. **1**, 100007 (2022). https://doi.org/10.1016/j.apmate.2021.09.007
59. Z. Liu, L. Li, L. Qin, S. Guo, G. Fang et al., Balanced interfacial ion concentration and migration steric hindrance promoting high-efficiency deposition/dissolution battery chemistry. Adv. Mater. **34**, e2204681 (2022). https://doi.org/10.1002/adma.202204681
60. Y. Pan, Z. Liu, S. Liu, L. Qin, Y. Yang et al., Quasi-decoupled solid–liquid hybrid electrolyte for highly reversible interfacial reaction in aqueous zinc–manganese battery. Adv. Energy Mater. **13**, 2203766 (2023). https://doi.org/10.1002/aenm.202203766
61. Y. Zhang, J. Xu, Z. Li, Y. Wang, S. Wang et al., All-climate aqueous Na-ion batteries using water-in-salt electrolyte. Sci. Bull. **67**, 161–170 (2022). https://doi.org/10.1016/j.scib.2021.08.010
62. C. Li, B. Liu, N. Jiang, Y. Ding, Elucidating the charge-transfer and Li-ion-migration mechanisms in commercial lithium-ion batteries with advanced electron microscopy. Nano Res. Energy **1**, e9120031 (2022). https://doi.org/10.2599/nre.2022.9120031
63. M. Chuai, J. Yang, M. Wang, Y. Yuan, Z. Liu et al., High-performance Zn battery with transition metal ions co-regulated electrolytic MnO_2. eScience **1**, 178–185 (2021). https://doi.org/10.1016/j.esci.2021.11.002
64. Y.-Y. Wang, X.-Q. Zhang, M.-Y. Zhou, J.-Q. Huang, Mechanism, quantitative characterization, and inhibition of corrosion in lithium batteries. Nano Res. Energy **2**, e9120046 (2023). https://doi.org/10.26599/nre.2023.9120046
65. L. Yuan, J. Hao, B. Johannessen, C. Ye, F. Yang et al., Hybrid working mechanism enables highly reversible Zn electrodes. eScience **3**, 100096 (2023). https://doi.org/10.1016/j.esci.2023.100096
66. H. Liu, F. Liu, Z. Qu, J. Chen, H. Liu et al., High sulfur loading and shuttle inhibition of advanced sulfur cathode enabled by graphene network skin and N, P, F-doped mesoporous carbon interfaces for ultra-stable lithium sulfur battery. Nano Res. Energy **2**, e9120049 (2023). https://doi.org/10.26599/nre.2023.9120049
67. X. Ji, A perspective of $ZnCl_2$ electrolytes: the physical and electrochemical properties. eScience **1**, 99–107 (2021). https://doi.org/10.1016/j.esci.2021.10.004
68. X. Guo, C. Wang, W. Wang, Q. Zhou, W. Xu et al., Vacancy manipulating of molybdenum carbide MXenes to enhance Faraday reaction for high performance lithium-ion batteries. Nano Res. Energy **1**, e9120026 (2022). https://doi.org/10.26599/nre.2022.9120026
69. X. Chen, P. Ruan, X. Wu, S. Liang, J. Zhou, Crystal structures, reaction mechanisms, and optimization strategies of MnO_2 cathode for aqueous rechargeable zinc batteries. Acta Phys. Chim. Sin. **38**(11), 2111003 (2021). https://doi.org/10.3866/pku.whxb202111003
70. Q. Liu, Y. Hu, X. Yu, Y. Qin, T. Meng et al., The pursuit of commercial silicon-based microparticle anodes for advanced lithium-ion batteries: a review. Nano Res. Energy **1**, e9120037 (2022). https://doi.org/10.26599/nre.2022.9120037
71. M. Wang, Y. Meng, K. Li, T. Ahmad, N. Chen et al., Toward dendrite-free and anti-corrosion Zn anodes by regulating a bismuth-based energizer. eScience **2**, 509–517 (2022). https://doi.org/10.1016/j.esci.2022.04.003
72. H. Ye, Y. Li, Towards practical lean-electrolyte Li–S batteries: highly solvating electrolytes or sparingly solvating electrolytes? Nano Res. Energy **1**, e9120012 (2022). https://doi.org/10.26599/nre.2022.9120012
73. Y. Liu, Y. Li, J. Sun, Z. Du, X. Hu et al., Present and future of functionalized Cu current collectors for stabilizing lithium metal anodes. Nano Res. Energy **2**, e9120048 (2023). https://doi.org/10.26599/nre.2023.9120048
74. W. Lv, J. Meng, X. Li, C. Xu, W. Yang et al., Boosting zinc storage in potassium-birnessite via organic-inorganic electrolyte strategy with slight N-methyl-2-pyrrolidone additive. Energy Storage Mater. **54**, 784–793 (2023). https://doi.org/10.1016/j.ensm.2022.11.011
75. Z. Pei, Symmetric is nonidentical: operation history matters for Zn metal anode. Nano Res. Energy **1**, e9120023 (2022). https://doi.org/10.26599/nre.2022.9120023
76. M. Song, C.-L. Zhong, Achieving both high reversible and stable Zn anode by a practical glucose electrolyte additive toward high-performance Zn-ion batteries. Rare Met. **41**, 356–360 (2022). https://doi.org/10.1007/s12598-021-01858-2
77. M. Gao, Z. Wang, D.G. Lek, Q. Wang, Towards high power density aqueous redox flow batteries. Nano Res. Energy **2**, e9120045 (2023). https://doi.org/10.26599/nre.2023.9120045
78. G. Liang, X. Li, Y. Wang, S. Yang, Z. Huang et al., Building durable aqueous K-ion capacitors based on MXene family. Nano Res. Energy **1**, e9120002 (2022). https://doi.org/10.26599/nre.2022.9120002
79. Z. Cai, J. Wang, Y. Sun, Anode corrosion in aqueous Zn metal batteries. eScience **3**, 100093 (2023). https://doi.org/10.1016/j.esci.2023.100093
80. H. Ge, X. Feng, D. Liu, Y. Zhang, Recent advances and perspectives for Zn-based batteries: Zn anode and electrolyte. Nano Res. Energy **2**, e9120039 (2023). https://doi.org/10.26599/nre.2023.9120039
81. L. Yan, Y.-E. Qi, X. Dong, Y. Wang, Y. Xia, Ammonium-ion batteries with a wide operating temperature window from–40 to 80 °C. eScience **1**, 212–218 (2021). https://doi.org/10.1016/j.esci.2021.12.002

 https://doi.org/10.1007/s40820-024-01334-3

82. L. Jiang, D. Dong, Y.-C. Lu, Design strategies for low temperature aqueous electrolytes. Nano Res. Energy **1**, e9120003 (2022). https://doi.org/10.26599/nre.2022.9120003
83. C. Guan, F. Hu, X. Yu, H.-L. Chen, G.-H. Song et al., High performance of $HNaV_6O_{16}{\cdot}4H_2O$ nanobelts for aqueous zinc-ion batteries with in situ phase transformation by $Zn(CF_3SO_3)_2$ electrolyte. Rare Met. **41**, 448–456 (2022). https://doi.org/10.1007/s12598-021-01778-1
84. M. Zhu, Cryogenic electrolytes and catalysts for zinc air batteries. Nano Res. Energy **2**, e9120038 (2023). https://doi.org/10.26599/nre.2023.9120038
85. Z. Wang, M. Zhou, L. Qin, M. Chen, Z. Chen et al., Simultaneous regulation of cations and anions in an electrolyte for high-capacity, high-stability aqueous zinc–vanadium batteries. eScience **2**, 209–218 (2022). https://doi.org/10.1016/j.esci.2022.03.002
86. X. Yu, F. Hu, Z.-Q. Guo, L. Liu, G.-H. Song et al., High-performance $Cu_{0.95}V_2O_5$ nanoflowersas cathode materials for aqueous zinc-ion batteries. Rare Met. **41**, 29–36 (2022). https://doi.org/10.1007/s12598-021-01771-8
87. W. Lv, J. Meng, Y. Li, W. Yang, Y. Tian et al., Inexpensive and eco-friendly nanostructured birnessite-type δ-MnO_2: a design strategy from oxygen defect engineering and K^+ pre-intercalation. Nano Energy **98**, 107274 (2022). https://doi.org/10.1016/j.nanoen.2022.107274
88. H.-Z. Ren, J. Zhang, B. Wang, H. Luo, F. Jin et al., A V_2O_3@N–C cathode material for aqueous zinc-ion batteries with boosted zinc-ion storage performance. Rare Met. **41**, 1605–1615 (2022). https://doi.org/10.1007/s12598-021-01892-0
89. Z. Liu, Y. Yang, S. Liang, B. Lu, J. Zhou, pH-buffer contained electrolyte for self-adjusted cathode-free Zn–MnO_2 batteries with coexistence of dual mechanisms. Small Struct. **2**, 2100119 (2021). https://doi.org/10.1002/sstr.202100119
90. Z. Meng, Z. Qiu, Y. Shi, S. Wang, G. Zhang et al., Micro/nano metal–organic frameworks meet energy chemistry: a review of materials synthesis and applications. eScience **3**, 100092 (2023). https://doi.org/10.1016/j.esci.2023.100092
91. Y. Song, P. Ruan, C. Mao, Y. Chang, L. Wang et al., Metal-organic frameworks functionalized separators for robust aqueous zinc-ion batteries. Nano-Micro Lett. **14**, 218 (2022). https://doi.org/10.1007/s40820-022-00960-z
92. C.-X. Xu, J.-J. Jiang, Electrolytes speed up development of zinc batteries. Rare Met. **40**, 749–751 (2021). https://doi.org/10.1007/s12598-020-01628-6
93. C. Li, X. Xie, H. Liu, P. Wang, C. Deng et al., Integrated 'all-in-one' strategy to stabilize zinc anodes for high-performance zinc-ion batteries. Natl. Sci. Rev. **9**, nwab177 (2021). https://doi.org/10.1093/nsr/nwab177
94. T. Sun, Q.-Q. Sun, Y. Yu, X.-B. Zhang, Polypyrrole as an ultrafast organic cathode for dual-ion batteries. eScience **1**, 186–193 (2021). https://doi.org/10.1016/j.esci.2021.11.003
95. Y. Tian, S. Chen, Y. He, Q. Chen, L. Zhang et al., A highly reversible dendrite-free Zn anode via spontaneous galvanic replacement reaction for advanced zinc-iodine batteries. Nano Res. Energy **1**, e9120025 (2022). https://doi.org/10.26599/nre.2022.9120025
96. W. Nie, H. Cheng, Q. Sun, S. Liang, X. Lu et al., Design strategies toward high-performance Zn metal anode. Small Meth. (2023). https://doi.org/10.1002/smtd.202201572
97. X. Gao, J. Li, Z. Zuo, Advanced electrochemical energy storage and conversion on graphdiyne interface. Nano Res. Energy **1**, e9120036 (2022). https://doi.org/10.26599/nre.2022.9120036
98. Z.-X. Zhu, Z.-W. Lin, Z.-W. Sun, P.-X. Zhang, C.-P. Li et al., Deciphering H^+/$Zn2^+$ co-intercalation mechanism of MOF-derived 2D MnO/C cathode for long cycle life aqueous zinc-ion batteries. Rare Met. **41**, 3729–3739 (2022). https://doi.org/10.1007/s12598-022-02088-w
99. M. Zhang, J. Yuan, Graphene meta-aerogels: when sculpture aesthetic meets 1D/2D composite materials. Nano Res. Energy **1**, e9120035 (2022). https://doi.org/10.26599/nre.2022.9120035
100. X. Chen, W. Li, Z. Zeng, D. Reed, X. Li et al., Engineering stable Zn–MnO_2 batteries by synergistic stabilization between the carbon nanofiber core and birnessite-MnO_2 nanosheets shell. Chem. Eng. J. **405**, 126969 (2021). https://doi.org/10.1016/j.cej.2020.126969
101. X. Li, Q. Zhou, Z. Yang, X. Zhou, D. Qiu et al., Unraveling the role of nitrogen-doped carbon nanowires incorporated with MnO_2 nanosheets as high performance cathode for zinc-ion batteries. Energy Environ. Mater. **6**, 12378 (2023). https://doi.org/10.1002/eem2.12378
102. A. Huang, J. Chen, W. Zhou, A. Wang, M. Chen et al., Electrodeposition of MnO_2 nanoflakes onto carbon nanotube film towards high-performance flexible quasi-solid-state Zn–MnO_2 batteries. J. Electroanal. Chem. **873**, 114392 (2020). https://doi.org/10.1016/j.jelechem.2020.114392
103. S. Islam, M.H. Alfaruqi, J. Song, S. Kim, D.T. Pham et al., Carbon-coated manganese dioxide nanoparticles and their enhanced electrochemical properties for zinc-ion battery applications. J. Energy Chem. **26**, 815–819 (2017). https://doi.org/10.1016/j.jechem.2017.04.002
104. C. Wang, Y. Zeng, X. Xiao, S. Wu, G. Zhong et al., γ-MnO_2 nanorods/graphene composite as efficient cathode for advanced rechargeable aqueous zinc-ion battery. J. Energy Chem. **43**, 182–187 (2020). https://doi.org/10.1016/j.jechem.2019.08.011
105. Z. Xiao, F. Xia, L. Xu, X. Wang, J. Meng et al., Suppressing the jahn–teller effect in Mn-based layered oxide cathode toward long-life potassium-ion batteries. Adv. Funct. Mater. **32**, 2108244 (2022). https://doi.org/10.1002/adfm.202108244
106. C. Zhou, D. Wang, A. Li, E. Pan, H. Liu et al., Three-dimensional porous carbon doped with N, O and P heteroatoms as high-performance anode materials for sodium ion batteries. Chem. Eng. J. **380**, 122457 (2020). https://doi.org/10.1016/j.cej.2019.122457
107. W. Chen, G. Li, A. Pei, Y. Li, L. Liao et al., A manganese-hydrogen battery with potential for grid-scale energy

storage. Nat. Energy **3**, 428–435 (2018). https://doi.org/10.1038/s41560-018-0147-7

108. J. Jin, Y. Liu, X. Zhao, H. Liu, S. Deng et al., Annealing in argon universally upgrades the Na-storage performance of Mn-based layered oxide cathodes by creating bulk oxygen vacancies. Angew. Chem. Int. Ed. **62**(15), e202219230 (2023). https://doi.org/10.1002/anie.202219230
109. Y. Cheng, Y. Jiao, P. Wu, Manipulating Zn 002 deposition plane with zirconium ion crosslinked hydrogel electrolyte toward dendrite free Zn metal anodes. Energy Environ. Sci. **16**(10), 4561–4571 (2023). https://doi.org/10.1039/D3EE02114A
110. S. Zhang, L. Sun, Q. Fan, F. Zhang, Z. Wang et al., Challenges and prospects of lithium-CO_2 batteries. Nano Res. Energy **1**(1), e9120001 (2022). https://doi.org/10.26599/NRE.2022.9120001
111. Z. Meng, Y. Jiao, P. Wu, Alleviating side reactions on Zn anodes for aqueous batteries by a cell membrane derived phosphorylcholine zwitterionic protective layer. Angew. Chem. Int. Ed. **62**(31), e202307271 (2023). https://doi.org/10.1002/anie.202307271
112. D. Feng, Y. Jiao, P. Wu, Proton-reservoir hydrogel electrolyte for long-term cycling Zn/PANI batteries in wide temperature range. Angew. Chem. Int. Ed. **62**(1), e202215060 (2023). https://doi.org/10.1002/anie.202215060
113. W. Li, Y. Ma, H. Shi, K. Jiang, D. Wang, Cu_7Te_4 as an anode material and Zn dendrite inhibitor for aqueous Zn-ion battery. Adv. Funct. Mater. **32**(38), 2205602 (2022). https://doi.org/10.1002/adfm.202205602
114. W. Liu, Z. Zhao, T. Li, S. Li, H. Zhang et al., A high potential biphenol derivative cathode: toward a highly stable air-insensitive aqueous organic flow battery. Sci. Bull. **66**(5), 457–463 (2021). https://doi.org/10.1016/j.scib.2020.08.042
115. W. Li, Y. Ma, P. Li, X. Jing, K. Jiang, D. Wang, Electrochemically activated $Cu_{2-X}Te$ as an ultraflat discharge plateau, low reaction potential, and stable anode material for aqueous Zn-ion half and full batteries. Adv. Energy Mater. **11**(42), 2102607 (2021). https://doi.org/10.1002/aenm.202102607
116. Y. Gao, B.-F. Cui, J.-J. Wang, Z.-Y. Sun, Q. Chen et al., Improving Li reversibility in Li metal batteries through uniform dispersion of Ag nanoparticles on graphene. Rare Met. **41**, 3391–3400 (2022). https://doi.org/10.1007/s12598-022-02044-8
117. W. Li, X. Jing, Y. Ma, M. Chen, M. Li et al., Phosphorus-doped carbon sheets decorated with SeS_2 as a cathode for aqueous Zn-SeS_2 battery. Chem. Eng. J. **420**(Part 1), 129920 (2021). https://doi.org/10.1016/j.cej.2021.129920
118. X. Xie, J. Li, Z. Xing, B. Lu, S. Liang et al., Biocompatible zinc battery with programmable electro-cross-linked electrolyte. Natl. Sci. Rev. **10**(3), nwac281 (2023). https://doi.org/10.1093/nsr/nwac281
119. S. Lei, Z. Liu, C. Liu, J. Li, B. Lu et al., Opportunities for biocompatible and safe zinc-based batteries. Energy Environ. Sci. **15**(12), 4911–4927 (2022). https://doi.org/10.1039/D2EE02267B
120. J. Li, P. Ruan, X. Chen, S. Lei, B. Lu et al., Aqueous batteries for human body electronic devices. ACS Energy Lett. **8**(7), 2904–2918 (2023). https://doi.org/10.1021/acsenergylett.3c00678

 https://doi.org/10.1007/s40820-024-01334-3